Cao, Q., Xu, Q., Lin, C.-H., Wei, D., Deng, Z., and Chen, Q. 2019. "Study of particle deposition on the complex components of environmental control systems," *International Journal of Heat and Mass Transfer*, 135: 1218-1232

Study of Particle Deposition on the Complex Components of Environmental Control Systems

Qing Cao[1], Qiuyu Xu[1], Chao-Hsin Lin[2], Daniel Wei[3], Zhipeng Deng[4], and Qingyan Chen[4*]

[1]Tianjin Key Laboratory of Indoor Air Environmental Quality Control, School of Environmental Science and Engineering, Tianjin University, Tianjin, China
[2]The Boeing Company, Seattle, USA
[3]Boeing Research & Technology-China, Beijing, China
[4]School of Mechanical Engineering, Purdue University, West Lafayette, IN, USA

[*]*Corresponding email: yanchen@purdue.edu*

Keywords*: CFD; Particle mass; Heat exchanger; Turbocharger; Lagrangian model; Turbulence model; Measurements.*

Abstract

As most airplanes do not have HEPA filters for filtering outside air, particulate matter in the outdoor air can deposit on the environmental control systems (ECS) of the airplanes. The particles that accumulate on the various surfaces of the ECS components can affect their thermal performance and may lead to component failures. This study experimentally and numerically investigated the particle deposition on a heat exchanger and a turbocharger, which are key components of ECS with complex geometry. A test rig was built to obtain the monodisperse particle deposition fractions by measuring the particle concentration upstream and downstream of the components with the weighing method. The tested particles ranged from 1 to 8 μm in diameter. Different Reynolds-averaged Navier-Stokes (RANS) models, together with a modified Lagrangian method, were used to predict the total particle deposition fractions in the tested components. The computed particle deposition was compared with the experimental data. The results showed that the RNG k-ε model with near-wall correction provided the most accurate prediction of the particle deposition fraction on the heat exchanger and turbocharger. The particle deposition fraction increased significantly with the particle size. CFD simulation provided detailed information about the particle deposition distribution inside the heat exchanger and turbocharger. The location and number of deposited particles depended mainly on the particle size and air velocity. This investigation identified a suitable tool for studying particle deposition in the ECS of commercial airplanes.

Highlights

- Experimental and numerical investigation of the particle deposition for different sizes in a plate-fin heat exchanger and a turbocharger.
- The particle deposition fraction increased with particle size on the plate-fin heat exchanger and the turbocharger.
- RNG k-ε model with near-wall correction provided the most accurate prediction of the particle deposition fraction on the heat exchanger and turbocharger.
- A suitable tool was identified for studying particle deposition in the ECS of commercial airplanes.
- The particle deposition distributions in the plate-fin heat exchanger and turbocharger were obtained with the CFD method to identify the location with highest fouling risk.

1. Introduction

Commercial airplanes use environmental control systems (ECS) to provide conditioned outside air to the cabin for maintaining a suitable air pressure and temperature [1]. However, most of these airplanes do not have HEPA filters for filtering outside air [2]. Airborne particulate matter from or close to the ground at heavily polluted airports could deposit on the surfaces of ECS components such as heat exchangers, condensers, fans, turbochargers and ducts [3]. Because of heavy traffic in the air, the ground operation time for mid-size airplanes can be comparable to that in the air [4]. The particles that accumulate on the various surfaces of the ECS components can affect their thermal performance and lead to component failures [5,6]. For example, the accumulated particulate fouling on heat exchangers may increase air-side thermal resistance and pressure drop, resulting in a significant deterioration of long-term heat-exchange performance [7,8]. Particle deposition may cause material wear on the fan blades of a turbine or compressor, degrading its aerodynamic performance [9]. The particle mass loading rate on an ECS component is a very important factor in its maintenance. Therefore, to assess the impact of particle accumulation on the ECS components, it is important to determine the particle deposition fraction.

Although some studies [10-12] have investigated particle deposition on air-conditioning systems in buildings, few have been conducted on particle deposition on ECS components in an airplane. Cao et al. [3] experimentally investigated the overall particle deposition fraction in the ECS of different commercial airplanes and showed that as much as 90% of PM2.5 could deposit on the ECS when the outside air quality on the ground was poor. Liu et al. [13] modeled particle deposition fractions on different parts of the ECS for different particle sizes using a set of empirical equations. The complex components, such as heat exchangers and turbochargers, in the air-conditioning pack of the ECS were simplified to very simple geometries, with the result that they under-predicted the particle deposition fraction. Particulate matter is more likely to be deposited on ECS components with complex geometry. However, there was no detailed information about the sizes or numbers of particles deposited on different components of the ECS.

The heat exchanger and air cycle machine are important parts of the air-conditioning pack in the ECS [14]. Compact cross-flow plate-fin heat exchangers are typically used in aircraft because of their high heat-exchange efficiency, small size and light weight [15]. In the air-conditioning pack, primary and secondary heat exchangers, which are of similar structure, are used for cooling bleed air [16]. The air cycle machine consists of a centrifugal compressor driven by a centrifugal turbine on a common shaft [17]. The performance of these components obviously influences the cooling efficiency of the ECS.

Our literature search identified few studies of particle deposition on these ECS components. For heat exchangers, most previous studies [18-20] have focused on particle deposition on the air side of the fin-and-tube heat exchangers typically used for HVAC systems in buildings, the geometric structures of which are different from the plate-fin heat exchangers used in ECS. Hosseini et al. [21,22] reported experimental and numerical data on the pressure drop caused by particle deposition in a compact heat exchanger. However, they conducted investigations on only five fin-channels rather than the whole heat exchanger. Since the header and distributor configuration of a compact heat exchanger always produces non-uniform flow distribution [23,24], the particle deposition on the whole heat exchanger would be different from that on the fin channels. For the air cycle machine, investigations have sought mainly to understand the

influence of particle fouling on the performance parameters of the tested component, such as mean flow coefficient and mean pressure-rise coefficient [25,26]. Few studies have addressed ways to determine the position of the deposited particles. Although several studies [27,28] investigated particle deposition on the blades of the air cycle machine, the results did not exactly represent the deposition in the whole component. It is therefore essential to study where and how many particles are deposited in the whole plate-fin heat exchanger and air cycle machine.

Both experimental measurements and numerical simulations can be used to investigate particle deposition. Experimental measurements can provide accurate data for validation of the numerical results. Computational fluid dynamics (CFD) simulations can provide detailed information about airflow, particle deposition and movement in ECS components with complex geometries. In recent years, Lagrangian methods have become very popular for calculating indoor particle deposition [29-32]. These methods track the trajectory of each particle, together with the airflow distribution calculated by means of CFD. Therefore, an appropriate turbulence model that simulates the airflow distribution is the key to correctly predicting particle deposition. To reduce the requirement for computing resources, many studies [28, 33-36] have used two-equation RANS turbulence models with the Lagrangian method to study particle deposition on devices with complex geometries. In those studies, the renormalization group (RNG) k-ε model [37], the realizable k-ε model [38] and the shear stress transport (SST) k-ω model [39] were most popular. In addition, the airflows in the heat exchanger and turbocharger were characterized by high swirl dominated flows. The three turbulence models are reported to be suitable for simulating this type of flow. Therefore, this study chose the three turbulence models for comparison. Nevertheless, it is unclear which of the turbulence models with a Lagrangian method could provide the most accurate prediction of particle deposition on complex ECS components, such as the plate-fin heat exchanger and air cycle machine.

Therefore, our study conducted both experimental and numerical studies of particle deposition on a plate-fin heat exchanger and an air cycle machine. The objective of this study was to identify the best turbulence model for use in CFD to predict the particle deposition. The simulated results were compared with the experimental data. The resulting numerical tool can be used to improve the design of ECS components for reduction of particle deposition or to determine when maintenance is needed.

2. Research Method

This section describes the rationale for selection of the ECS components; the process for measuring the particle deposition fraction on the ECS components; and the numerical procedure that was used for calculating the particle deposition on the ECS components.

2.1 Selection of the tested components

To identify the most valuable ECS components for investigation, it was essential to understand the working principle of the air-conditioning pack, which controls the air pressure and temperature in the aircraft cabin. As shown in Fig. 1, the air-conditioning pack of a commercial airplane consists of the following components: pack valve, heat exchangers, air cycle machine, water separator, low temperature limit (35°F) system, etc. The air-conditioning process is as follows [40]: A portion of the bleed air travels through the primary heat exchanger and is cooled by the ram air. Next, the cooled bleed air enters the compressor section of the air cycle machine, where the air is compressed to a higher pressure; the process also increases the air temperature. The hot compressed air then passes through a secondary heat exchanger for

additional cooling before it is expanded in the turbine section of the air cycle machine to cool the air further. These stages comprise a reversed Brayton cycle for cooling. Next, the water separator collects and removes the water condensed from the air before it mixes with the other portion of the bleed air in the mix chamber to form suitable pressure and temperature for delivery to the cabin. As can be seen in Fig. 1, the heat exchangers and air cycle machine are the key ECS components.

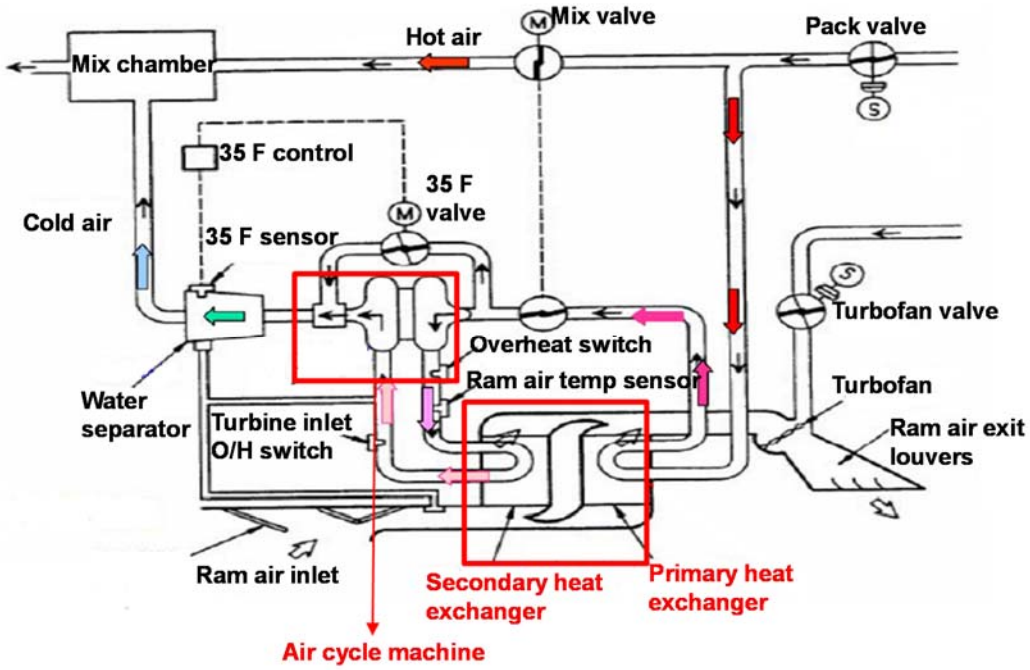

Fig. 1. The working principle of the air-conditioning pack

In addition, because of the complex geometry of the heat exchanger and air cycle machine, particles are more likely to deposit on these components. Therefore, this study selected the heat exchanger and air cycle machine for investigation of particle deposition. Since it is difficult to obtain components that are identical to those used in aircraft, we used a plate-fin heat exchanger and a turbocharger, as shown in Fig. 2. Although the experimentally studied components differed in size and weight from the heat exchangers and air cycle machine actually used in ECS, the studied components had the same working principles and structures.

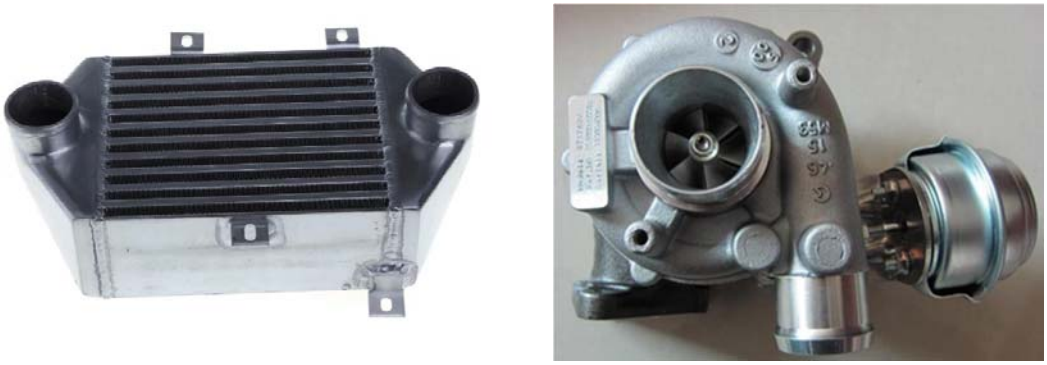

(a) (b)

Fig. 2. (a) The heat exchanger and (b) the turbocharger selected for this study

2.2 Measurements of particle deposition on the heat exchanger and turbocharger

In order to determine the particle deposition on the heat exchanger and turbocharger, a test rig was built to obtain the monodisperse particle deposition fractions of particles ranging from 1 to 8 μm in diameter. Because of the narrow spaces and complex structures of the two components, this investigation measured the particle concentration upstream and downstream of the components with the weighing method. To provide an isothermal condition, the experiments were conducted in an air-conditioned laboratory, where the air temperature was controlled at about 20□. During the experiments, there were no heat sources in the test rig. Fig. 3 shows a schematic and photographs of the test rig, which included a HEPA filter to filter particles in the incoming air, a particle generator (MAG 3000) that generated monodisperse particles of the desirable diameter, a mixing box to enhance the particle and air mixing, two sampling boxes in which particle concentrations were measured, the tested component (the heat exchanger or the turbocharger), and a centrifugal fan to control the flow rate through the component. The type of HEPA we chose in this study is GY-A-3-320×320×292-500. The category is A and the filter can remove at least 99.9% of particles 0.3 μm in diameter from the air passing through the filter. The particle generator released monodisperse particles made of DEHS (Di-Ethyl-Hexyl-Sebacat), with diameters ranging from 1 to 8 μm. This study used an aerodynamic particle sizer (APS from TSI Inc., Model 3320) to measure the particle size in the upstream sampling box. APS was only used to identify the size of particles generated by the particle generator. The only one of its kind available on the market, the TSI APS measures the aerodynamic size of particles from 0.5 to 20 μm. It offers high size resolution, one-second sampling, and real-time size distributions. The individual particle deposition fraction was measured by a more accurate way of weighing method. The particle mass in the air was collected upstream and downstream of the tested component by isokinetic sampling of the air onto polytetrafluoroethylene filter paper. The reason for choosing this sampling filter is that it has hydrophobic characteristics, which can prevent the water vapor in the air in the experimental environment from affecting the experimental results. An electronic analytical balance (AND HM-202) with an accuracy of 0.01 mg was used to weigh the mass gain of the filter paper after sampling for one hour. A hot-sphere anemometer (AirDistSys5000) with a precision of 0.02 m/s was used to measure the air velocity before the sampling filter in the sampling box. The sampling flow rate can be calculated based on the measured air velocity. A flow rate controller (ALICAT) with a precision of ±0.01 L/min was used to control the flow rate through the sampling filter to achieve the isokinetic sampling. The flow rate through the test component was obtained by the tracer gas decay method. As shown in the literature [20, 41, 42], one of the main factors in particle deposition is the air velocity. This investigation set the air velocity through the heat exchanger and turbocharger to be the same as that for the ECS. With the assumption of a B737-800 airplane with 164 seats, the inlet air velocities of the heat exchanger and turbocharger were 21.9 m/s and 47.2 m/s, respectively. The rotating speed of the turbocharger wheel was 3120 rpm.

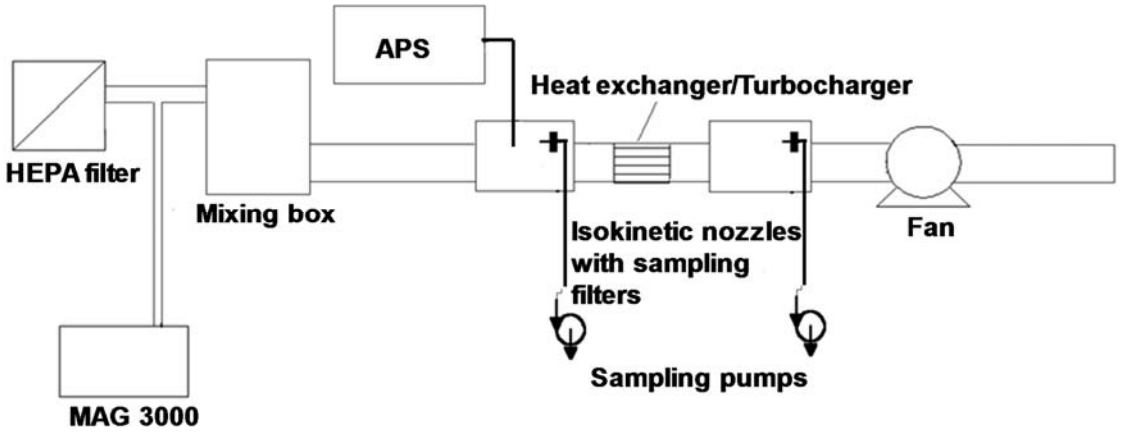

(a)

(b)

Fig. 3. (a) Schematic and (b) photographs of the experimental rig

The particle deposition fraction on the test component can be calculated by:

$$P_{deposition} = 1 - \frac{C_{downstream}}{C_{upstream}} = 1 - \frac{\Delta m_{downstream}/(G_{downstream} \times t)}{\Delta m_{uptream}/(G_{upstream} \times t)} \quad (1)$$

where $P_{deposition}$ is the particle deposition fraction on the test component; $C_{downstream}$ is the particle concentration downstream of the test component, g/m^3; $C_{upstream}$ is the particle concentration upstream of the test component, g/m^3; $\Delta m_{downstream}$ is the mass gain of the filter in the downstream sampling box, g; $\Delta m_{upstream}$ is the mass gain of the filter in the upstream sampling box, g; $G_{downstream}$ is the sampling volume flow rate in the downstream sampling box, m^3/s; $G_{upstream}$ is the sampling volume flow rate in the upstream sampling box, m^3/s; and t is the sampling time, s.

2.3 Numerical method

This investigation used different Reynolds-averaged Navier-Stokes (RANS) models and a modified Lagrangian particle-tracking method to predict the total particle deposition fractions on the tested components. The computed results for particle deposition were then compared with the experimental data obtained in this study. Finally, the particle deposition distribution was analyzed in detail.

2.3.1 Brief description of the turbulence models

This study assessed the ability of three commonly used two-equation RANS turbulence models, the RNG k-ε model, the realizable k-ε model and the SST k-ω model, to predict airflow in a plate-fin heat exchanger and a turbocharger. The RNG k-ε model calculates turbulence kinetic energy (k) and its dissipation rate (ε) by two independent transport equations. The model is isotropic but very stable. The realizable k-ε model proposed by Shih et al. [38] was intended to address the deficiencies of traditional k-ε models by adopting a new eddy-viscosity formula involving a variable C_μ originally proposed by Reynolds [43]. The model also uses a dissipation rate equation (ε) based on the dynamic equation of the mean-square vorticity fluctuation. The SST k-ω model calculates turbulence kinetic energy (k) and its specific dissipation rate (ω), again by two independent transport equations. The model applies the standard k-ω model in the near-wall region and the transformed k-ε model in the free shear region [40]. The transport equations of the turbulence models can be written in a general format as follows [44]:

$$\rho\frac{\partial\bar{\Phi}}{\partial t}+\rho\bar{u}_i\frac{\partial\bar{\Phi}}{\partial x_i}-\frac{\partial}{\partial x_i}\left[\Gamma_{\phi,eff}\frac{\partial\bar{\Phi}}{\partial x_i}\right]=S_\phi \tag{2}$$

where, ϕ is a specific variable, $\Gamma_{\phi,eff}$ the coefficient of effective diffusion, and S_ϕ the source term of the general equation. The corresponding parameters for the turbulence models used in this study are summarized in Table 1.

Table 1 Summary of coefficients of Equation (2).

Equation or model		ϕ	$\Gamma_{\phi,eff}$	S_ϕ	Constants
Reynolds-averaged variables	Continuity	1	0		
	Momentum	u_j	$\mu+\mu_t$	$-\frac{\partial p}{\partial x_i}+\frac{\partial}{\partial x_j}\left[(\mu+\mu_t)\frac{\partial u_j}{\partial x_i}\right]$	
	Temperature	T	$\frac{\mu}{Pr}+\frac{\mu_t}{\sigma_T}$	S_T	
RNG k-ε		k	$\mu+\frac{\mu_t}{\sigma_k}$	$G_k+G_b-\rho\varepsilon$	$\mu_t=\rho C_\mu\frac{k^2}{\varepsilon}, G_K=\mu_t S^2$, S = $\sqrt{2S_{ij}S_{ij}}$ $G_b=\beta g_i\frac{\partial\mu_t}{\partial\sigma_{T,t}}\frac{\partial\bar{T}}{\partial x_i}$, $R_\varepsilon=\frac{C_\mu\rho\eta^3(1-\eta/\eta_0)}{1+\beta\eta^3}\frac{\varepsilon^2}{k}$, $\eta\equiv Sk/\varepsilon$, $\eta_0=4.38$, $\beta=0.012$, $\sigma_k=1.0$, $\sigma_\varepsilon=1.3$, $C_\mu=0.0845$, $C_{1,\varepsilon}=1.42$, $C_{2,\varepsilon}=1.68$
		ε	$\mu+\frac{\mu_t}{\sigma_\varepsilon}$	$C_{1\varepsilon}G_k\frac{\varepsilon}{k}-C_{2\varepsilon}\rho\frac{\varepsilon^2}{k}-R_\varepsilon$	
Realizable k-ε		k	$\mu+\frac{\mu_t}{\sigma_k}$	$G_k+G_b-\rho\varepsilon$	$\mu_t=\rho C_\mu\frac{k^2}{\varepsilon}, G_k=\mu_t S^2$, $S=\sqrt{2S_{ij}S_{ij}}$ $G_b=\beta g_i\frac{\partial\mu_t}{\partial\sigma_{T,t}}\frac{\partial\bar{T}}{\partial x_i}$, $C_1=max\left[0.43,\frac{\eta}{\eta+5}\right]$, $\eta=Sk/\varepsilon$, $C_\mu=\frac{1}{A_0+A_S(kU*/\varepsilon)}$,
		ε	$\mu+\frac{\mu_t}{\sigma_\varepsilon}$	$\rho C_1 S_\varepsilon-\rho C_2\frac{\varepsilon^2}{k+\sqrt{\upsilon\varepsilon}}$	

				$U* \equiv \sqrt{S_{ij}S_{ij} + \tilde{\Omega}_{ij}\tilde{\Omega}_{ij}}$, $\sigma_k = 1.0$, $\sigma_\varepsilon = 1.2$, $C_{1,\varepsilon} = 1.44$, $C_2 = 1.9$
SST k-ω	k	$\mu + \frac{\mu_t}{\sigma_k}$	$G_k - Y_k$	$\mu_t = \frac{\rho k}{\omega}\frac{1}{max[(1/\alpha*), SF_2/a_1\omega]}$ $\sigma_k = \frac{1}{\frac{F_1}{\sigma_{k,1}} + \frac{(1-F_1)}{\sigma_{k,2}}}$, $\sigma_\omega = \frac{1}{\frac{F_1}{\sigma_{\omega,1}} + \frac{(1-F_1)}{\sigma_{\omega,2}}}$, $G_k = \mu_t S^2$, $G_\omega = \frac{\alpha}{\nu_t}\tilde{G}_k$, $\tilde{G}_k = min(G_k, 10\rho\beta^* k\omega)$, $Y_k = \rho\beta^* k\omega$, $Y_\omega = \rho\beta\omega^2$, $\sigma_{k,1} = 1.176$, $\sigma_{\omega,1} = 2.0$, $\sigma_{k,2} = 1.0$, $\sigma_{\omega,2} = 1.168$, $a_1 = 0.31$
	ω	$\mu + \frac{\mu_t}{\sigma_\omega}$	$G_\omega - Y_\omega$	

2.3.2 Particle movement model

This investigation used the Lagrangian method to track individual particle motion directly on the basis of the airflow distribution calculated from CFD with the turbulence models. The turbulent flow field is treated as a continuous phase and simulated in the Eulerian frame. As reported by the literature [45], the Saffman's force and Brownian force only have effect on sub-micron particles, this investigation did not consider them in the particle movement equation. The Lagrangian method determines the particle model in accordance with Newton's law:

$$\frac{du_p}{dt} = \frac{18\mu_a}{\rho_p d_p^2 C_c}\left(u_a - u_p\right) + \frac{g(\rho_p - \rho_a)}{\rho_p} \quad (3)$$

where the first and second terms on the right-hand side represent the drag force and gravity term, respectively, μ_α air viscosity, d_p particle diameter, u_p particle velocity, u_a air velocity, g gravitational acceleration, ρ_p particle density, ρ_a air density, and C_c the Cunningham correction factor. The factor can be expressed as:

$$C_c = 1 + \frac{2\lambda}{d_p}(1.257 + 0.4exp(-1.1d_p/2\lambda)) \quad (4)$$

where λ is the mean free path of air molecules.

Particle turbulent dispersion, which is associated with instantaneous flow fluctuations, is one of the main mechanisms of particle deposition. This study used the discrete random walk (DRW) model to calculate the particle turbulent dispersion. The DRW model simulates the interaction of a particle with a succession of discrete stylized fluid-phase turbulent eddies. Each eddy is characterized by a Gaussian distributed random-velocity fluctuation, u_i', v_i' and w_i'. The u_i', v_i' and w_i' that prevail during the lifetime of the turbulent eddy are sampled by assuming that they obey a Gaussian probability distribution.

The RNG k-ε model, realizable k-ε model and SST k-ω model assume the turbulent fluctuations to be isotropic. Thus, the turbulent fluctuating velocity can be calculated as:

$$u_i' = \zeta_i \sqrt{\overline{u_i'^2}} = \zeta_i \sqrt{2k/3} \quad (5)$$

where ζ_i is a standard normal random number.

With the above equations, one can determine particle trajectory in turbulence flow including turbulence dispersion. Proper simulation of the turbulent fluctuating velocity in the near-wall region is crucial to particle deposition modeling. However, the turbulent fluctuating velocity in the near-wall region simulated by the RANS models is less accurate than the direct numerical simulation, which is rarely used in practice because of the significant requirement for computing resources [46]. Previous studies [47,48] adopted curve-fitted direct numerical simulations to correct the turbulent fluctuating velocity in the near-wall region. For the two-equation models, the RNG k-ε model, realizable k-ε model and SST k-ω model, near-wall corrections have been used for the turbulence kinetic energy because of the assumption of isotropic turbulence. Jiang et al. [49] incorporated the findings from Wang and James [50] and proposed the following equation to modify the turbulence kinetic energy in the near-wall region ($y^+ \leq 80$):

$$k_{near\_wall} = [1 - exp(-0.02y^+)]^2 k \quad (6)$$

where y^+ is the dimensionless wall distance, $y^+ = yu^*/v$; u* friction velocity, m/s; ν the kinematic viscosity of air, m^2/s; and y the distance from the cell to the nearest wall.

2.3.3 Particle deposition velocity modeling

To better understand where and how many particles deposited on the surfaces of the test components, this investigation calculated the local particle deposition velocity on a given computing mesh, i, by [31]:

$$v_{d,i} = \frac{N_{d,i}/(A_i \cdot t)}{\overline{N}/V} \quad (7)$$

where A_i is the area of the local computing mesh, $N_{d,i}$ the number of particles depositing onto this mesh within the time t, $\overline{N}$ the average number of particles in the calculated space within t, and V the volume of the inner space in the test components. Chen et al. (2016) [47] found that 4 time constants could obtain consistent and accurate results. Therefore, this study calculated for 4 time constants of the heat exchanger and turbocharger to obtain the particle deposition results.

3. Case Setup

Fig. 4 shows the geometric model of the heat exchanger and turbocharger used for the CFD simulation. Because of the symmetric geometry, only half of the heat exchanger was modeled to reduce calculation time. Since the impellers in the turbocharger were rotating at a speed of 3120 rpm, this study used the multi-reference frame (MRF) approach to consider the rotating motion. This approach, which has also been used by Jiao et al. [51] and Coroneo et al. [52], keeps the mesh stationary and simulates the motion by using a rotating coordinate system to lower the computational cost [53]. The blue section shown in Fig. 4(b) was the rotating zone. The impellers were set to be the moving walls, while the other walls were stationary. The

calculation domain was extended 500 mm at the inlet and 200 mm at the outlet of the tested components to obtain fully developed flow and to avoid reversed flow. The inlet velocity was uniform and set to 21.9 m/s and 45.2 m/s for the heat exchanger and turbocharger, respectively; these values were the same as those in the experiment. For the heat exchanger, a turbulent intensity of 3.9% and a length scale of 58 mm (equal to the diameter of the inlet) were used for the inlet boundary conditions. For the turbocharger, the turbulent intensity was 4.1% and the length scale 18.4 mm.

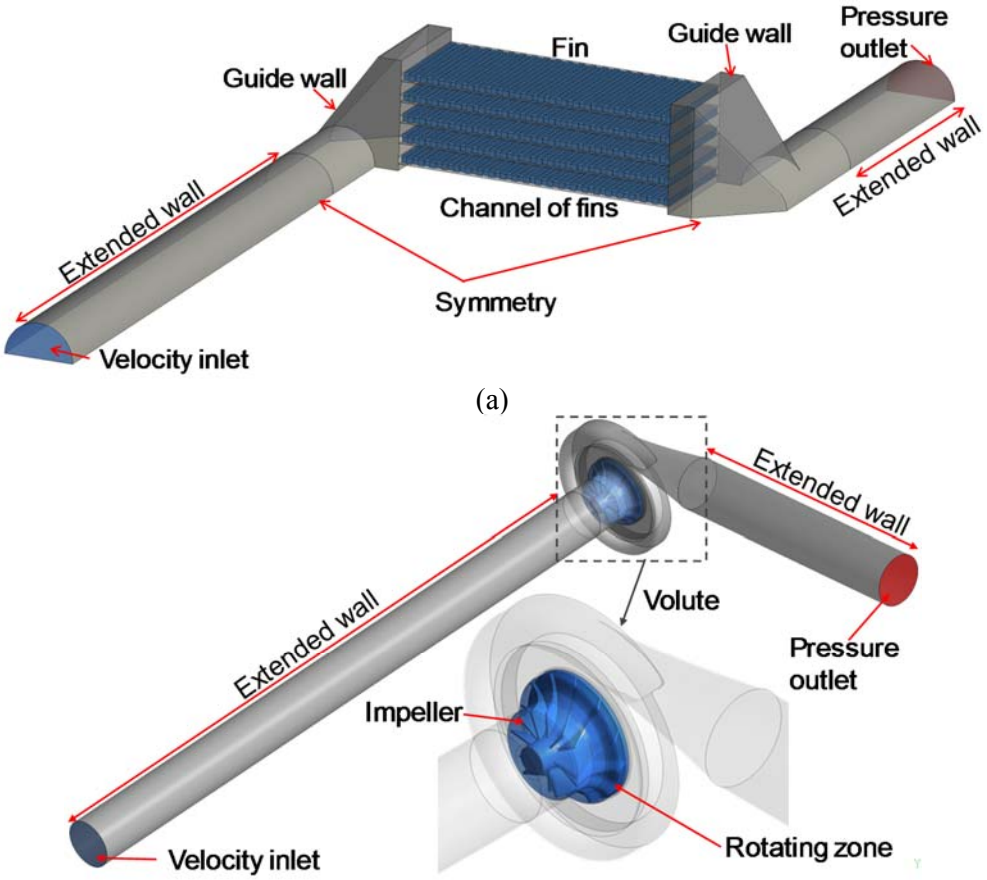

Fig. 4. Computational domain and boundary conditions used in this study (a) for the plate-fin heat exchanger and (b) for the turbocharger

This study used tetrahedral grids throughout the whole computational domain. For both the heat exchanger and turbocharger, three grid resolutions were tested. Fig. 5 shows the facet average velocity on a cross section of the heat exchanger and turbocharger simulated by different grids. For heat exchanger, 0.57, 1.52 and 4.43 million grids were tested, and it was found that grid number of 1.52 million provided grid-independent results. For turbocharger, this study compared the results of 0.42, 1.07 and 2.34 million grids and found that 1.07 million was sufficient.

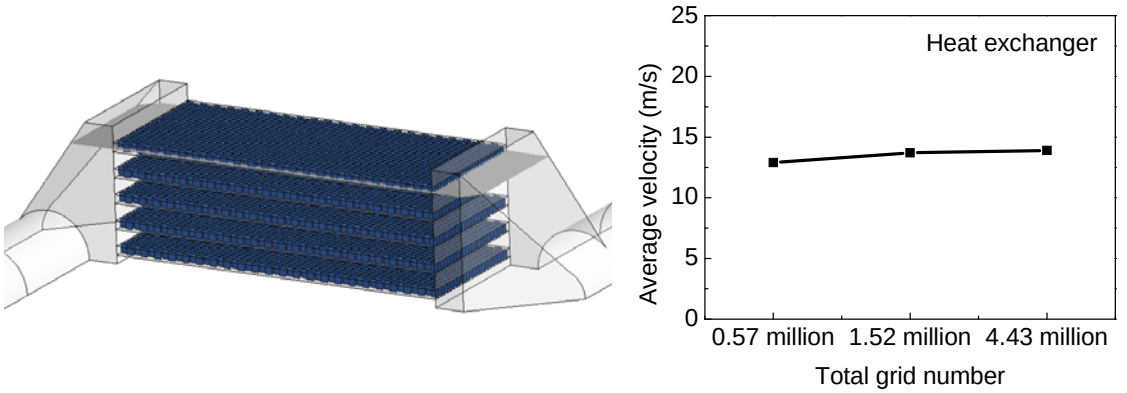

(a)

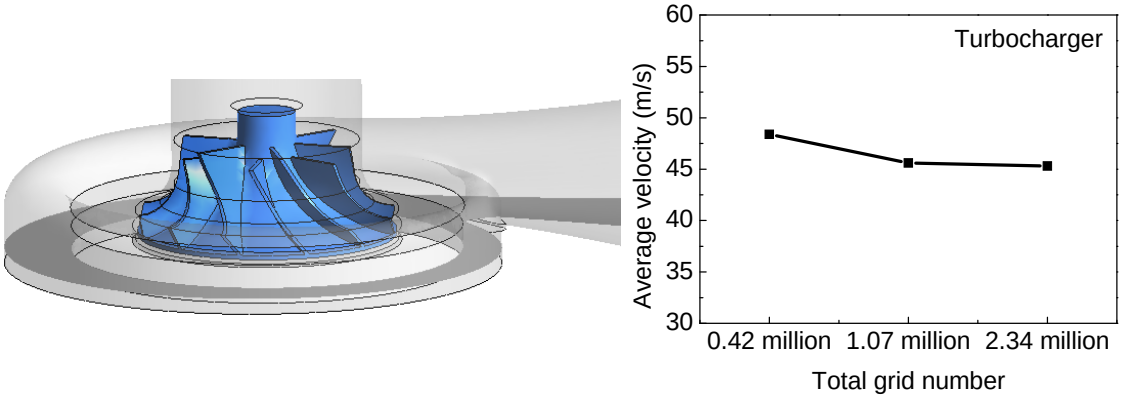

(b)

Fig. 5. Location of the cross section and face average velocity simulated by different grids (a) for the plate-fin heat exchanger and (b) for the turbocharger

Elghobashi (1994) [54] concluded when the volume fraction of particle (V_p/V) smaller than 10^{-6}, the particles had a negligible effect on the flow turbulence. A one-way coupling can be used between the dispersed and continuous phase. We calculated the maximum volume fraction of particles used in the simulation, which is equal to 2.7×10^{-11}. Since the particle concentration investigated in this study was low, the effect of particles on the turbulence could be neglected. One-way coupling seems appropriate for the interaction between the airflow and particles. The particle density was 912 kg/m^3. This study selected the velocity inlet as the surface injection to release the monodisperse spherical inert particles. To obtain a statistical particle deposition result, 100,000 spherical particles were uniformly released at the inlet with a velocity equal to the inlet air velocity in each case. As the particles usually cannot accumulate enough rebound energy to overcome the adhesion force, this study assumed no particle resuspension in the simulations. When the particles passed through the outlet, the calculations of the trajectory were terminated, and the particles escaped from the component.

Fig. 6 shows the size distributions of the monodisperse particles with diameters of 2.4 μm and 5.1 μm that were generated by the particle generator. The monodisperse diameter was the weighted average of the particle size distribution. Note that eight different particle sizes were used in the experiment, and the diameter distributions for all sizes were similar to those shown in Fig. 6. The relationship between the particle concentration and the aerodynamic diameter was a skewed normal distribution. The particles diameter distribution was sufficiently concentrated to be regarded as monodisperse. Therefore, in the CFD modeling, the particle

deposition fraction in the heat exchanger or turbocharger for each diameter was calculated as Eq. (8):

$$P_{deposition,CFD} = 1 - \frac{N_{out}}{N_{in}} \tag{8}$$

where, N_{out} and N_{in} are the particle number at the outlet and inlet of the heat exchanger or turbocharger, respectively.

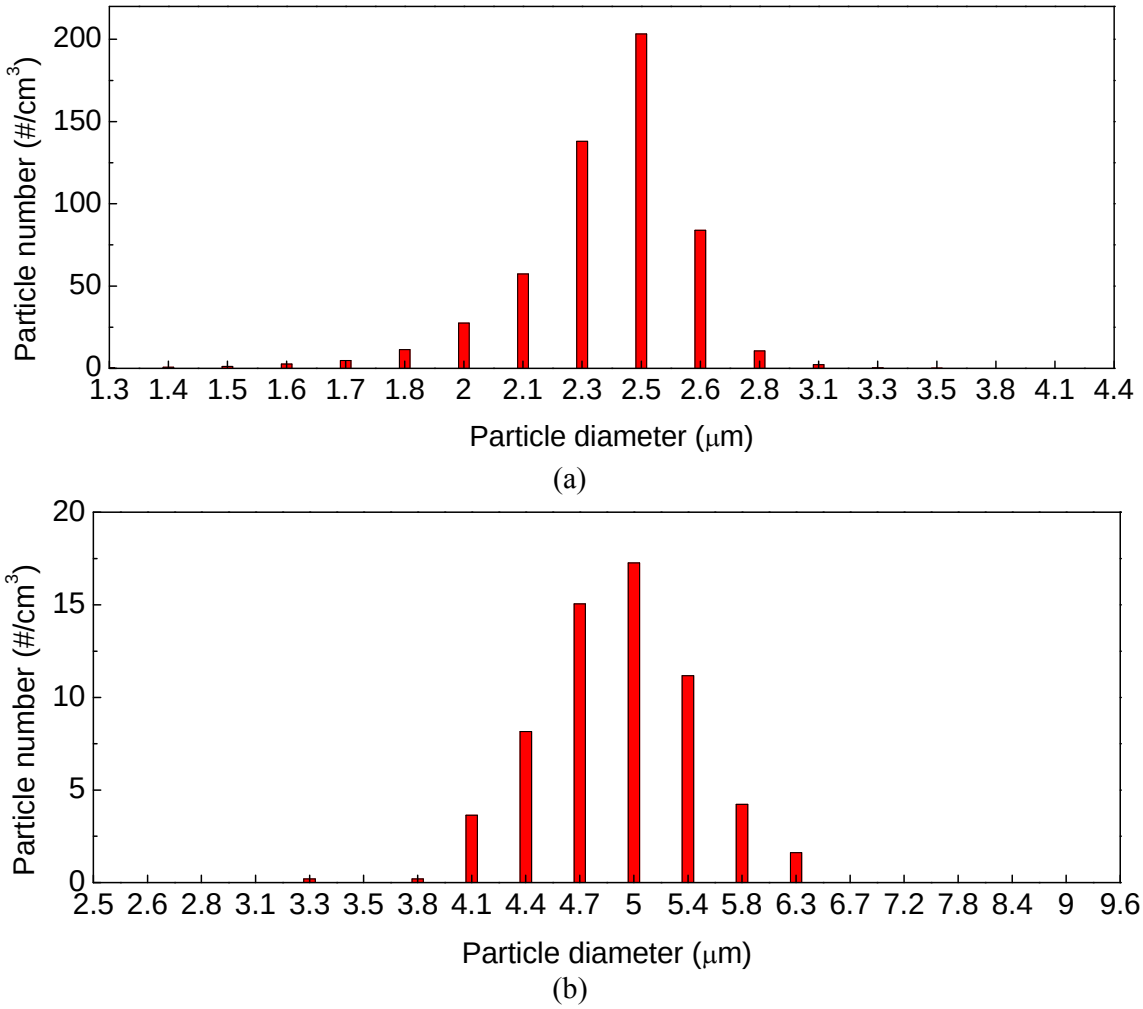

Fig. 6. The size distribution of the particles measured by the aerodynamic particle sizer for monodisperse diameters of (a) 2.4 μm and (b) 5.1 μm in CFD modeling.

This study used a commercial CFD program, ANSYS Fluent 16.0, to calculate the airflow field and particle trajectories. At first, in the calculation, the airflow field was calculated with the turbulence models. Then, the near-wall correction function was employed to correct the turbulence kinetic energy in the near-wall regions. Next, particles were uniformly released from the inlet into the calculation domain. Then, Lagrangian tracking method was used to calculate the particle movement trajectories and the particle deposition velocities. The near-wall turbulence correction and the calculation of particle deposition velocity were implemented by user-defined functions. The particle deposition fraction was calculated with the numbers of deposited and released particles using Eq. (8). The governing equations for the airflow were solved by the finite volume method. The SIMPLE algorithm was used for pressure and velocity

coupling of the transport equations, and second-order discretization schemes were used for solving all the independent variables. Convergence of all the variables' normalized residuals was reached at 10^{-4}. Table 2 summarizes the CFD settings.

Table 2 Summary of CFD methods and boundary conditions

Item		Heat exchanger	Turbocharger
Mesh		1.52 million	1.07 million
Near-wall function		Standard wall function	
Average wall Y^+		21.9	56.2
Inlet velocity		21.95 m/s	45.22 m/s
Inlet turbulent intensity		3.90%	4.10%
Inlet length scale		58 mm	18.4 mm
No-slip stationary walls		Extended wall; fins; guide wall	Extended wall; volute
No-slip moving walls		/	Impeller
Outlet		Pressure outlet	
Discretization	Pressure	PRESTO!	
	Momentum	Second order upwind	
	Turbulent kinetic energy	Second order upwind	
	Turbulent dissipation rate	Second order upwind	
Particle density		912 kg/m^3	
Particle trajectories		100,000	
Particle size		1.0, 2.4, 3.2, 4.4, 5.1, 6.5, 7.2, 8.1 μm	
Particle injection type		Surface	
Time step size for particle tracking		0.0001 s	
Others	Rotating treatment	/	MRF approach
	Rotating speed	/	3120 rpm

4. Results

This investigation used the research method described in Section 2 to study the cases shown above. This section reports the results obtained from the study.

4.1 Flow field and particle simulations for the heat exchanger

Fig. 7 shows the airflow distribution in a cross section and a longitudinal section of the heat exchanger predicted by the three turbulence models. The SST k-ω model provided the smallest vortex in the inlet guide section and a slightly more uniform airflow distribution than the other two models. The flow distribution at the cross section (the interface of the guide section and fin channel inlets) was non-uniform because of the guide section. For the five fin channels, the inlet velocities differed from one another. Within each fin channel, the velocity distribution was non-uniform, which means that the particle fouling level varied among the five fin channels. Detailed information about particle deposition in the heat exchanger could be obtained by using Eq. (6) to model the particle deposition velocity on each computing mesh at the surfaces. Unfortunately, it was hard to obtain the experimental airflow distribution in the heat exchanger, and therefore this study did not compare the calculated flow with experimental data.

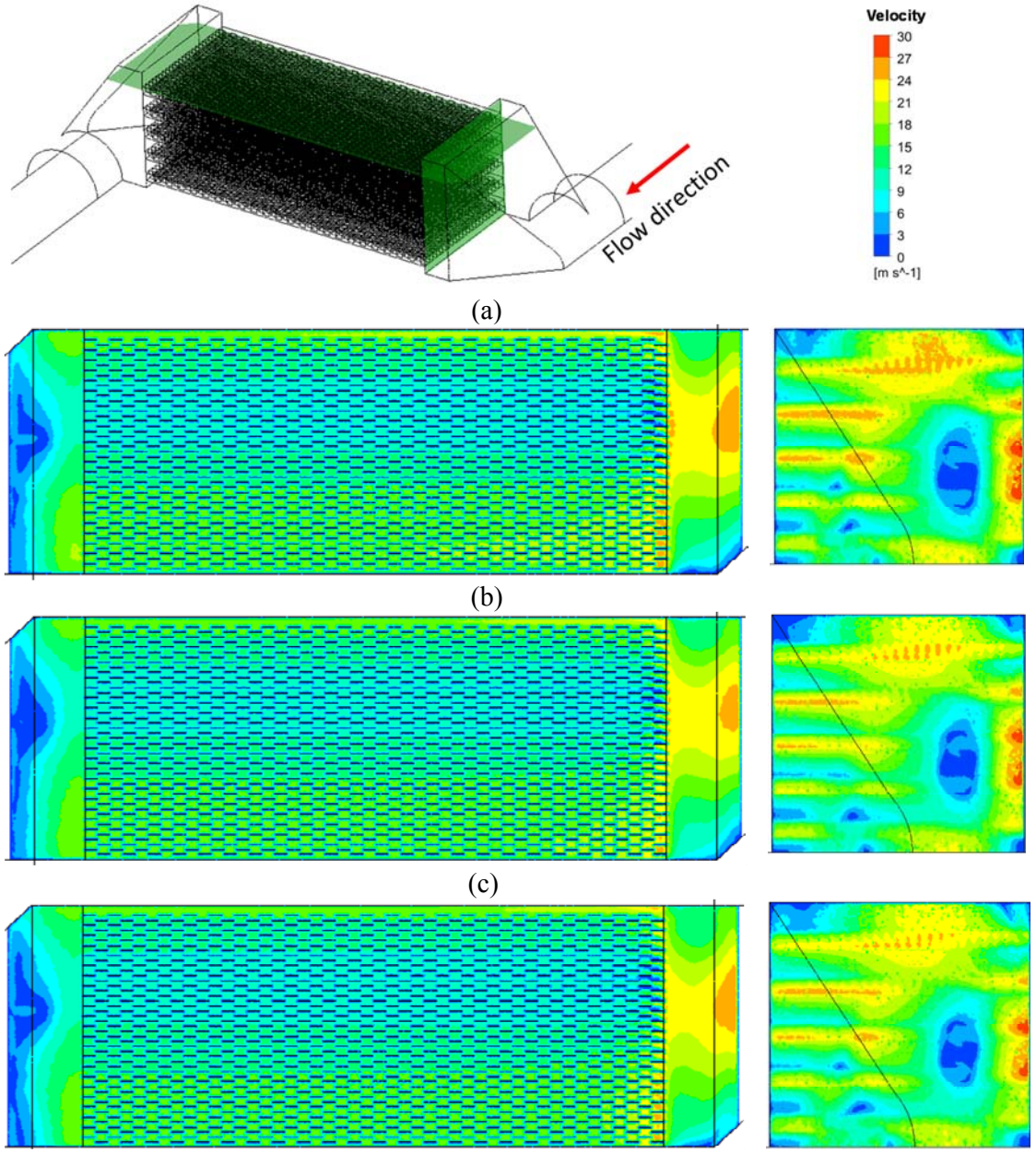

Fig. 7. Comparison of the airflow fields (a) in the cross section and longitudinal section of the heat exchanger predicted by (b) the RNG k-ε model, (c) the realizable k-ε model and (d) the SST k-ω model.

Fig. 8 shows the turbulence kinetic energy distribution in a cross section and a longitudinal section of the heat exchanger predicted by the three turbulence models. The turbulence kinetic energy distributions at the cross section and the longitudinal section were non-uniform, and the turbulence level in the guide section was higher than that in the fin channels. Unlike the airflow fields, the differences of turbulence kinetic energy simulated was obvious among the three turbulence models. The average turbulence kinetic energy of realizable k-ε model was the

highest and SST k-ω model was the lowest. As the particle deposition in the heat exchanger was mainly forced by the turbulence diffusion, the turbulence kinetic energy had a major impact on the particle deposition. Fig. 9 shows that the particle deposition fraction simulated by realizable k-ε model was also the highest and by SST k-ω model the lowest when the near-wall correction was not applied.

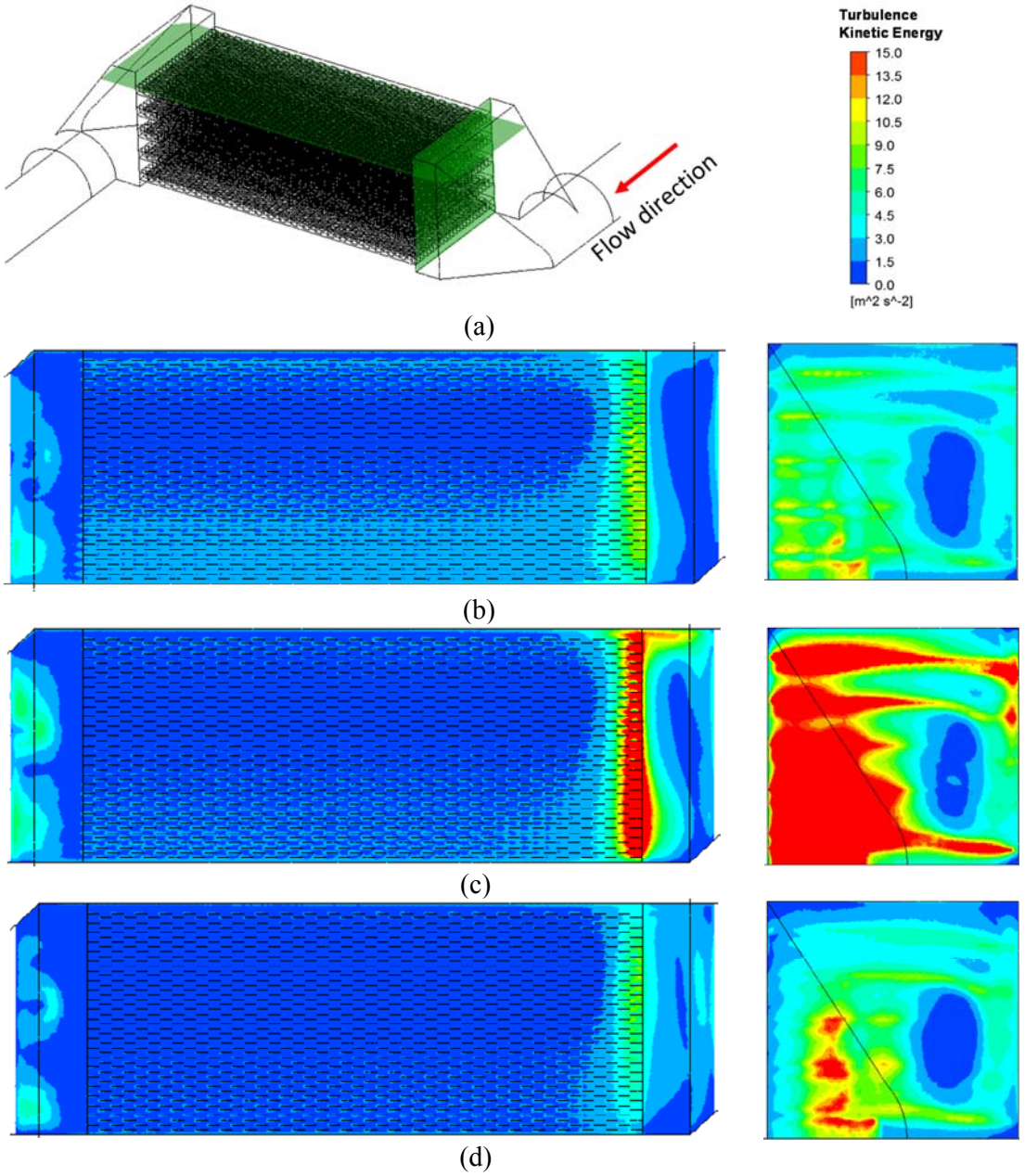

Fig. 8. Comparison of the turbulence kinetic energy fields (a) in the cross section and longitudinal section of the heat exchanger predicted by (b) the RNG k-ε model, (c) the realizable k-ε model and (d) the SST k-ω model.

This study compared the total particle deposition fraction in the heat exchanger predicted by three different turbulence models and also compared the simulation results with the measurement data. Fig. 9 shows the measured and simulated particle deposition fractions in the heat exchanger. For each particle size, the measurements were repeated three times to ensure

the validity of the experiment. The relative errors of the repetitive measurements for each particle size were less than 10%. The particle deposition fraction on the heat exchanger increased with the particle size. The deposition rate was 10% for 1 μm particles and 95% for 8 μm particles. Our measured deposition rate was much higher than that reported in the literature. For example, Siegel and Nazaroff [20] experimentally studied the particle deposition in the fin-and-tube heat exchangers with a face air velocity of 5.2 m/s. They found that the particle deposition fraction increased from 3% to 32% when the particle size changed from 1 μm to 8 μm. The difference was caused by the more complex geometry of the heat exchanger and the higher air velocity (9 m/s) used in the present study than in their study. The particle deposition fraction increases with high particle inertia and strong air turbulence. The trend of the simulated results was similar to that of the experimental data. Without the near-wall corrections, the particle deposition fractions predicted by the three turbulence models were higher than the experimental data, especially for particles with a diameter smaller than 3.8 μm. For particles with a diameter larger than 5.1 μm, the predictions by all three models agreed very well with the measurement data, both with and without the near-wall correction. The near-wall correction clearly improved the deposition rates simulated by the three turbulence models, and the RNG k-ε model produced the most accurate particle deposition fraction in the plate-fin heat exchanger. The SST k-ω model over-predicted the particle deposition fraction for most particle sizes, even with the near-wall correction, and this outcome may not be suitable for modeling the particle deposition on the plate-fin heat exchanger. The average relative errors between the simulated and measured deposition rates for the particles at eight different diameters were approximately 4.9%, 17.9% and 33.4% for the RNG k-ε model, realizable k-ε model and SST k-ω model, respectively.

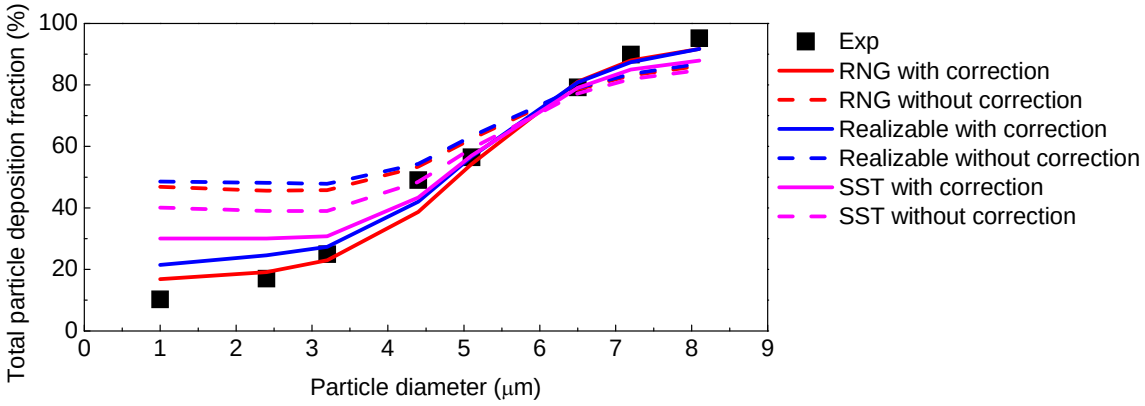

Fig. 9. Comparison of the particle deposition fraction in the heat exchanger predicted by different turbulence models with the measurement data.

To obtain detailed information about the location, number and size of the particles deposited on the surfaces of the plate-fin heat exchanger, this study calculated the deposition velocities for monodisperse particles according to Eq. (7). Since the RNG k-ε model with a near-wall correction predicted the most accurate total particle deposition fraction, this study adopted the model to calculate the local particle deposition velocity on each computational cell near the surfaces. Fig. 10 shows the predicted particle deposition velocity distributions onto the surfaces of the heat exchanger for particles with diameters of 1.0 μm, 3.2 μm, 6.5 μm and 8.1 μm. It can be seen that the deposition patterns varied with the particle diameter. For small particles, the deposition distribution was uniform on the fins and guide walls, which may have been caused predominantly by turbulence dispersion. Large particles were likely to deposit by impact on the

fins and inlet guide wall of the heat exchanger. The particles deposited mainly on the inlet guide wall and near the position connecting the fin channels with the inlet guide wall. In the fin channels, the deposition distribution was similar to the airflow pattern shown in Fig. 7. Higher velocities led to more deposition by impact. Large particles contributed significantly to the bulk of the fouling because of their size and high deposition fraction. For the plate-fin heat exchanger investigated here, the fouling risk was highest near the inlets of the fin channels.

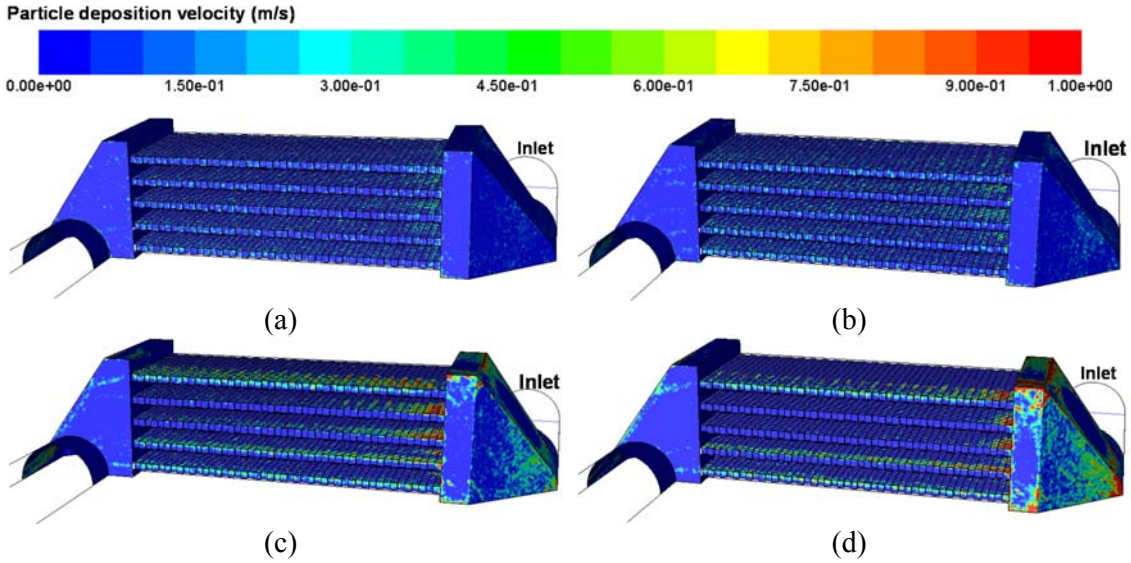

Fig. 10. Predicted patterns of particle deposition velocity on the inner surfaces of the plate-fin heat exchanger for particles with diameters of (a) 1.0 μm, (b) 3.2 μm, (c) 6.5 μm, and (d) 8.1 μm.

4.2 Flow field and particle simulations for the turbocharger

For the turbocharger, we also compared the simulation results obtained by using the three turbulence models. Fig. 11 shows the flow field in a cross section of the turbocharger. As the inlet velocities exceeded 40 m/s at times, the rotating impeller did not provide enough centrifugal force to produce a clockwise or counterclockwise rotating flow field. The high-speed flow hit the impeller directly and then spread out along the radial direction of the impeller. The highest velocity was found at the outlet of the volute. The air flow fields predicted by the three turbulence models were similar in most areas of the turbocharger, but a little differences were observed at the position connecting the volute and extended pipe.

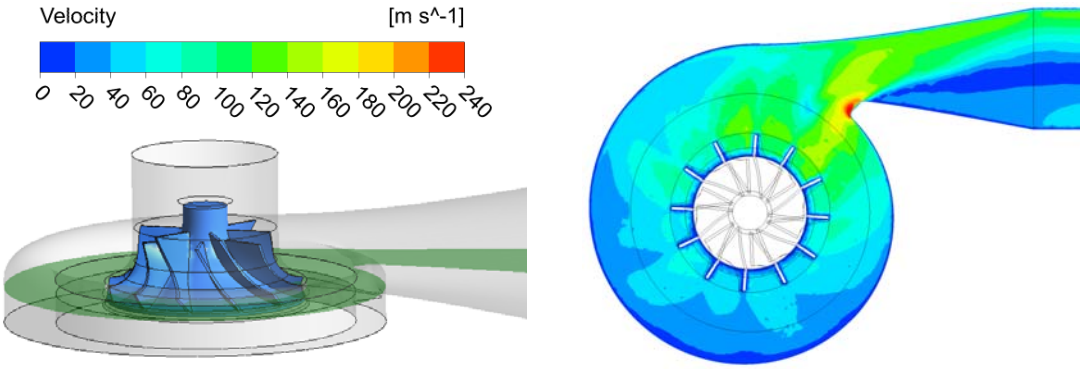

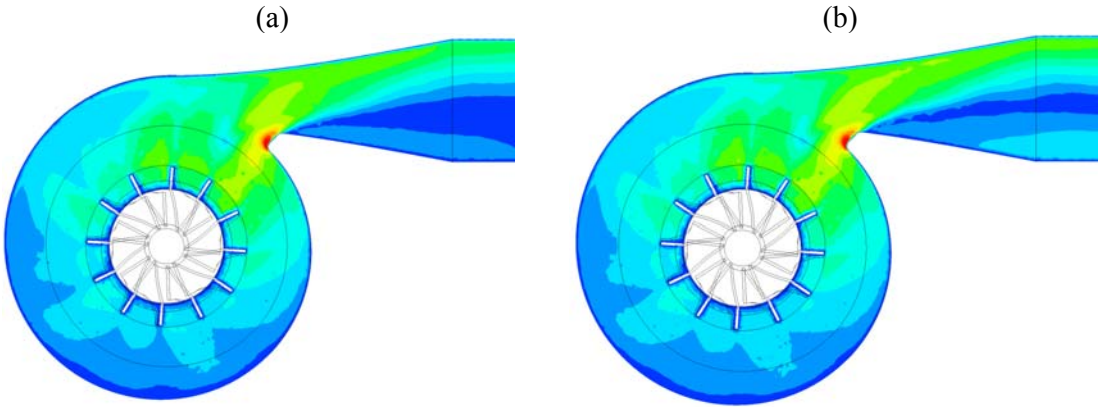

(a) (b) (c) (d)

Fig. 11. Comparison of the airflow fields (a) in the section of the turbocharger predicted by (b) the RNG k-ε model, (c) the realizable k-ε model and (d) the SST k-ω model.

Fig. 12 shows the turbulence kinetic energy distributions simulated by the three turbulence models in a cross section of the turbocharger. For all the three turbulence models, the highest turbulence level appeared at the outlet of the volute, where several flow steams met and mixed to generate strong turbulence. The average turbulence kinetic energy simulated by the realizable k-ε model was the highest and RNG k-ε model the lowest.

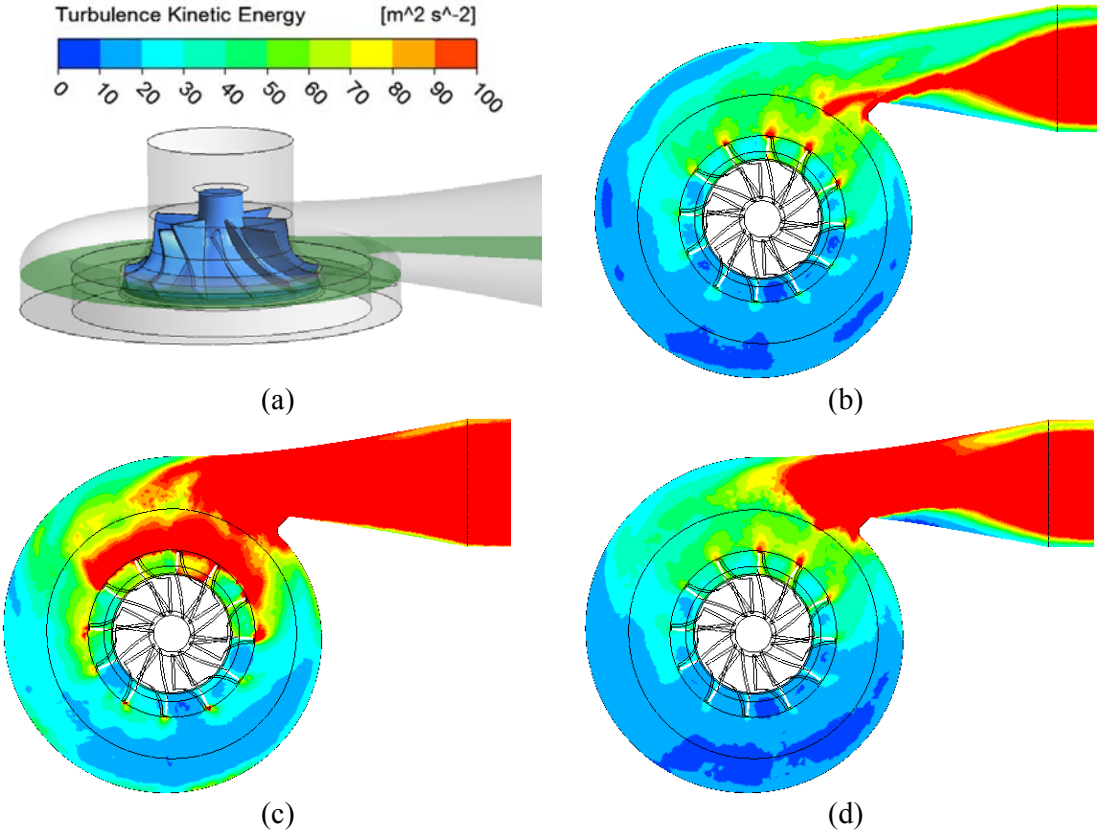

(a) (b) (c) (d)

Fig.12.Comparison of the turbulence kinetic energy fields(a) in the section of the turbocharger predicted by(b)the RNG k-ε model, (c)the realizable k-ε model and (d)the SST k-ω model.

Fig. 13 depicts the measured and simulated particle deposition fractions on the turbocharger. The deposition rate again increased with the particle size. However, the deposition rate on the

turbocharger was higher than that on the heat exchanger. Since the inlet air velocity of the turbocharger was 45.2 m/s, the inertial force in the turbocharger was much higher than that in the heat exchanger. When the turbocharger rotated at a speed of 3120 rpm, the rotating impeller increased the particle deposition. The particle deposition fraction was 32.9% for 1 μm particles and 89.3% for 8 μm particles. For the turbocharger, the particle deposition fractions simulated by the three turbulence models were close to the experimental data. As investigated by others [55, 56], turbulence diffusion significantly affected particle deposition in the "Brownian" and "transition" regions, while little effect on the particles in the "inertia region". The near wall corrections which calibrated the turbulence fluctuation level had no obvious effects on particles with very high velocities in the turbocharger in the "inertia region". For particles with very high velocities, the particle deposition was mainly caused by inertial impaction. The airflow fields simulated by the three turbulence models were similar. Therefore, the results simulated with and without near-wall corrections were similar. The average relative errors between the simulated and measured deposition rates were about 0.9%, 1.9% and 1.3% for the RNG k-ε model, realizable k-ε model and SST k-ω model, respectively; these errors were negligible.

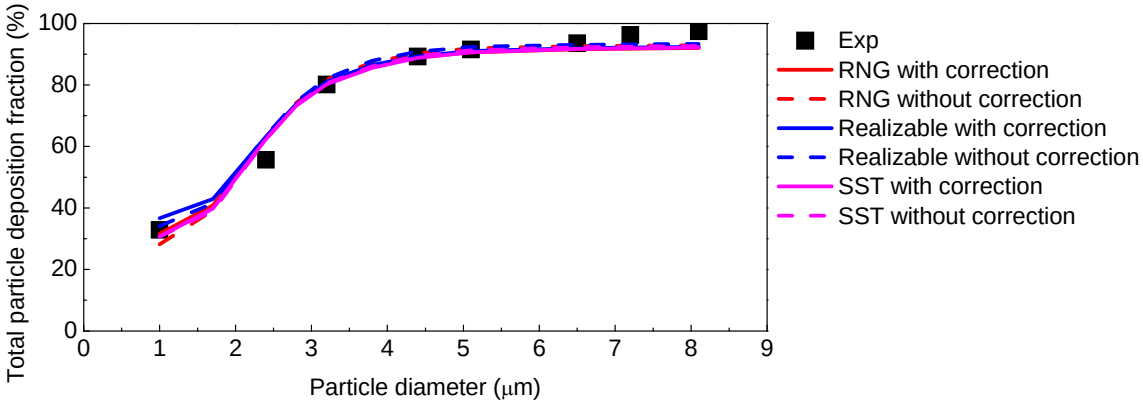

Fig. 13. Comparison of the particle deposition fraction in the turbocharger predicted by different turbulence models with the measurement data.

As with the heat exchanger, this study calculated the particle deposition velocity distributions in the turbocharger for particles of different sizes. Since the three turbulence models provided similar predictions of deposition rate, this study used the RNG k-ε model to calculate the particle deposition velocity distributions. Fig. 14 shows the particle deposition velocity distributions for four particle sizes. The deposition of 1 μm particles was fairly uniform, while the deposition of large particles occurred on the impeller. Therefore, the impeller has the highest fouling risk. For each diameter, the particle deposition in the turbocharger was higher than in the heat exchanger.

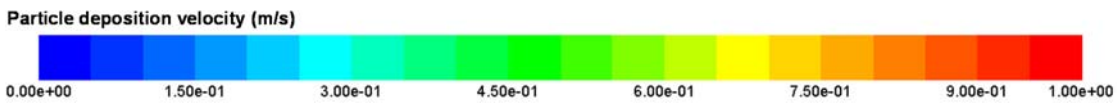

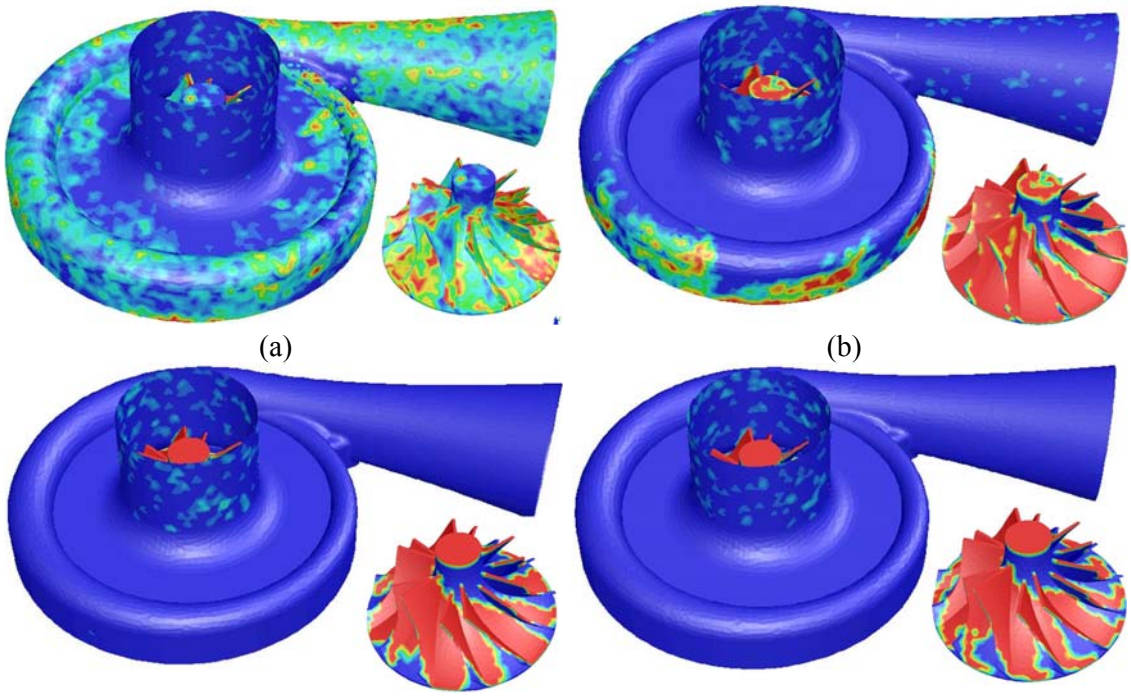

Fig. 14. Predicted pattern of particle deposition velocity on the inner surfaces of the turbocharger for particles with diameters of (a) 1.0 μm, (b) 3.2 μm, (c) 6.5 μm, and (d) 8.1 μm.

5. Discussion

This study modeled particle deposition under isothermal conditions with an air temperature of 293 K. However, the heat exchangers in the aircraft ECS may operate at a temperature as high as 500 K. Yang et al. [57] experimentally investigated the effect of temperature on PM2.5 deposition in a rectangular duct. They found that radial force thermophoresis pushed the particles toward the cold wall and enhanced the PM2.5 deposition. The deposition fraction increases with an increase in the difference between the air temperature and the cold wall temperature. Since the heat exchangers in the aircraft ECS are used to cool the hot bleed air, the actual particle deposition in the heat exchangers during operation may be higher than that predicted in this study.

This study used liquid particles made of DEHS to conduct the experiments, which adhere to a surface on contact. Kang et al., (2015) [58] experimentally studied the particle rebound fraction of liquid and solid particles to evaluate the effect of particle phase on particle bounce. They found that almost no liquid particles would rebound from surface. Matthew et al. (2008) [59] also reported that nearly 100% of liquid and liquid-coated particles were captured once they reached the surfaces. To compare with our experimental data, this study set that the particles were trapped once they reached the walls in the CFD modeling. References [60,61] reported that the particle rebound behavior may influenced by many factors, such as size, density, phase, hardness, hygroscopicity, impact velocity, surface materials, etc. In the atmosphere, there are different types of particles with different physical properties. The rebound behaviors of these particles were difficult to identify. And no detail database has been found to provide the rebound fraction, which can be set in the CFD modeling. Therefore, this study preferred to provide the worst case of particle deposition in the components. The information

is crucial for aircraft maintenance. Therefore, this study did not consider particle bounce and resuspension that were safe factors for the maintenance.

There are some nanoscale particles in bleed air, however, the mass of these particles was too small to have an obvious effect on the mass accumulation of deposited particles. For the particles with large diameters, most of them will deposit on the surfaces of the ducts before going through the air-conditioning pack. As investigated by Liu et al., (2017) [13], more than 90% of the particles with diameter larger than 10 μm deposited on the ducts before entering the air-conditioning pack. Most of the large particles have no chance to go through the components in the air-conditioning pack. Therefore, this study focused on the monodisperse particles with diameters ranged from 1 to 8 μm.

The sizes of the heat exchanger and turbocharger used in this study may be different from the sizes of the actual components used in the ECS of a commercial airplane. The impact of component size on particle deposition fraction was not examined. Furthermore, the measurements were conducted under isothermal and isobaric conditions, so that the effects of heat transfer and pressure on the deposition were neglected. In reality, the temperature and pressure in the ECS is quite different with the standard condition, the variation of particle size on different temperature and pressure conditions were not considered in this study, which needs more future work.

6. Conclusions

This investigation sought to numerically study the deposition rate of particulate matter in outside air on the key components of the environmental control system of a commercial airplane, i.e., a heat exchanger and a turbocharger. The study also performed experimental measurements of the overall deposition rates for comparison with the numerical results. The following conclusions were reached:

This study employed three commonly used two-equation RANS turbulence models with a Lagrangian method to predict particle deposition in the heat exchanger and turbocharger. The simulated results were compared with the experimental data obtained in this study. The comparison of measured and simulated particle deposition fraction showed that all the three turbulence models provided good prediction of particle deposition in the turbocharger, while for the heat exchanger the RNG k-ε model performed better than the other two models after applying the near-wall correction. Both the SST k-ω model and realizable k-ε model still overpredicted the particle deposition even with the near-wall correction. The limitation of realizable k-ε model was that it produced non-physical turbulent viscosities in some situations. The SST k-ω model can over-predict shear stresses of adverse pressure gradient boundary layers and that the model had issues predicting turbulence levels and complex internal flows. The model is also very sensitive to inlet boundary conditions, which is a disadvantage not seen in RNG k-ε model. Therefore, the RNG k-ε model with a near-wall correction together with the Lagrangian method is recommended for modeling particle deposition in the complex ECS components.

Both the experimental and numerical results show that the particle deposition fraction increased with particle size on the plate-fin heat exchanger and the turbocharger. Because of the complex geometry of the plate-fin heat exchanger, the measured deposition rate was 10.3% for 1 μm particles and 95.2% for 8 μm particles. Since the turbocharger rotated at a speed of 3120 rpm, the rotating impeller significantly enhanced the particle deposition fraction. Because

the inlet air velocity was as high as 45.2 m/s, generating a very significant impact on the particles, the measured deposition rate was 32.9% for 1 μm particles and nearly 97.5% for 8 μm particles. The averaged relative errors between the simulated and measured particle deposition fraction at eight different diameters are 4.9% and 0.9% in heat exchanger and turbocharger, respectively.

According to the simulated results in this study, particle deposition was high in both the plate-fin heat exchanger and the turbocharger, and the deposition distribution was non-uniform, especially for large particles. For the heat exchanger, the particles accumulated mainly at the inlet guide section and near the position connecting the fin channels with the inlet guide wall. The inlets of the five fin channels may be the first positions to be blocked by the particles. For the turbocharger, the impeller had the highest fouling risk, as most of the large particles deposited here.

Acknowledgement

The research presented in this paper was partially supported by the National Key R&D Program from the Ministry of Science and Technology, China, on "Green Buildings and Building Industrialization" through Grant No. 2016YFC0700500.

References

[1] Y. Tu, G. P. Lin, Dynamic simulation of aircraft environmental control system based on flowmaster. J Aircraft. 48.6 (2011) 2031-2041.
[2] K. Bull, Cabin air filtration helping to protect occupants from infectious diseases. Travel Med Infect Di. 6.3 (2008) 142-144.
[3] Q. Cao, Y. Liu, W. Liu, C.H. Lin, D. Wei, S. Baughcum, S. Norris, X. Shen, Z. Long, Q. Chen, Experimental study of particle deposition in the environmental control systems of commercial airliners. Build Environ. 96 (2016) 62-71.
[4] Q. Cao, Q. Xu, W. Liu, C.H. Lin, D. Wei, S. Baughcum, S. Norris, Q. Chen, In-flight monitoring of particle deposition in the environmental control systems of commercial airliners in China. Atmos Environ. 154 (2017) 118-128.
[5] J. Ma, C. Lu, H. Liu, Fault diagnosis for the heat exchanger of the aircraft environmental control system based on the strong tracking filter. PloS one 10.3 (2015) e0122829.
[6] U. Igie, M. Goiricelaya, D. Nalianda, O. Minervino, Aero engine compressor fouling effects for short-and long-haul missions. Proceedings of the Institution of Mechanical Engineers, Part G J Aerospace Eng. 230.7 (2016) 1312-1324.
[7] Y.C. Ahn, J.M. Cho, H.S. Shin, Y.J. Hwang, C.G. Lee, J.K. Lee, H.U. Lee, T.W. Kang, An experimental study of the air-side particulate fouling in fin-and-tube heat exchangers of air conditioners. Korean J Chem Eng. 20.5 (2003) 873-877.
[8] H. Pu, G.L. Ding, X.K. Ma, H.T. Hu, Y.F. Gao, Effects of biofouling on air-side heat transfer and pressure drop for finned tube heat exchangers. Int J Refrig. 32.5 (2009) 1032-1040.
[9] A. Corsini, F. Rispoli, A.G. Sheard, K. Takizawa, T.E. Tezduyar, P. Venturini, A variational multiscale method for particle-cloud tracking in turbomachinery flows. Comput Mech. 54.5 (2014) 1191-1202.
[10] F. Zhan, J. Tang, G. Ding, D. Zhuang, Experimental investigation on particle deposition characteristics of wavy fin-and-tube heat exchangers. Appl Therm Eng. 99 (2016) 1039-1047.
[11] B.A. Qureshi, S.M. Zubair. The impact of fouling on performance of a vapor compression

refrigeration system with integrated mechanical sub-cooling system. Appl Energ. 92 (2012) 750-762.
[12] M.S. Waring, J.A. Siegel, Particle loading rates for HVAC filters, heat exchangers, and ducts. Indoor Air, 18(3) (2008) 209-224.
[13] Y. Liu, Q. Cao, W. Liu, C.H. Lin, D. Wei, S. Baughcum, S. Norris, X. Shen, Z. Long, Q. Chen, Numerical modeling of particle deposition in the environmental control systems of commercial airliners on ground. Build Simul. Vol. 10. No. 2. Tsinghua University Press, 2017.
[14] D.V. Mahindru, P. Mahendru, Environmental Control System for Military and Civil Aircraft. Global J Res Eng. 11.5_D (2011).
[15] T.J. Leo, I. Pérez-Grande, A thermoeconomic analysis of a commercial aircraft environmental control system. Appl Therm Eng. 25.2-3 (2005) 309-325.
[16] J.V. Vargas, A. Bejan, Thermodynamic optimization of finned crossflow heat exchangers for aircraft environmental control systems. Int J Heat Fluid Fl. 22.6 (2001) 657-665.
[17] A. P. P. Santos, C. R. Andrade, E. L. Zaparoli. A thermodynamic study of air cycle machine for aeronautical applications. Int J Thermophys. 17.3 (2014) 117-125.
[18] H.V. Inamdar, E.A. Groll, J.A. Weibel, S.V. Garimella, Prediction of air-side particulate fouling of HVAC&R heat exchangers. Appl Therm Eng. 104 (2016) 720-733.
[19] J.M.R. Nasr, A. Balaei, Analysis of fouling in HVAC heat exchangers by CFD. Iran J Chem Chem Eng. 34.3 (2015) 51-60.
[20] J. A. Siegel, W. W. Nazaroff, Predicting particle deposition on HVAC heat exchangers. Atmos Environ. 37.39-40 (2003) 5587-5596.
[21] S.B. Hosseini, R.H. Khoshkhoo, S.J. Malabad, Experimental and numerical investigation on particle deposition in a compact heat exchanger. Appl Therm Eng. 115 (2017) 406-417.
[22] S.B. Hosseini, R.H. Khoshkhoo, S.J. Malabad, Numerical study on polydisperse particle deposition in a compact heat exchanger. Appl Therm Eng. 127 (2017) 330-346.
[23] J. Wen, Y. Li, Study of flow distribution and its improvement on the header of plate-fin heat exchanger. Cryogenics 44.11 (2004) 823-831.
[24] C. C. Wang, K.S. Yang, J.S. Tsai, Y. Chen, Characteristics of flow distribution in compact parallel flow heat exchangers, Part II: Modified inlet header. Appl Therm Eng. 31.16 (2011) 3235-3242.
[25] D. Fouflias, A, Gannan, K, Ramsden, P. Pilidis, D. Mba, J. Teixeira, U. Igie, P. Lambart, Experimental investigation of the influence of fouling on compressor cascade characteristics and implications for gas turbine engine performance. P I Mech Eng A-J Pow. 224.7 (2010) 1007-1018.
[26] G. Jombo, J. Pecinka, S. Sampath, D. Mba, Influence of fouling on compressor dynamics experimental and modeling approach. Journal of Engineering for Gas Turbines and Power 140.3 (2018) 032603.
[27] A. Suman, M. Morini, R. Kurz, N, Aldi, K. Brun, M. Pinelli, P.R. Spina, Quantitative computational fluid dynamics analyses of particle deposition on a transonic axial compressor blade—Part I: Particle zones impact. J Turbomach. 137.2 (2015) 021009.
[28] S. Saxena, G. Jothiprasad, C. Bourassa, B. Pritchard, Numerical simulation of particulates in multistage axial compressors. J Turbomach. 139.3 (2017) 031013.
[29] J. Bouilly, K. Limam, C. Béghein, F. Allard, Effect of ventilation strategies on particle decay rates indoors: An experimental and modelling study. Atmos Environ. 39.27 (2005) 4885-4892.
[30] A.C.K. Lai, F. Chen, Modeling particle deposition and distribution in a chamber with a two-equation Reynolds-averaged Navier–Stokes model. J Aerosol Sci. 37.12 (2006) 1770-1780.
[31] Z. Zhang, Q. Chen, Prediction of particle deposition onto indoor surfaces by CFD with a

modified Lagrangian method. Atmos Environ. 43.2 (2009) 319-328.
[32] M. Wang, C.H. Lin, Q. Chen, Determination of particle deposition in enclosed spaces by Detached Eddy Simulation with the Lagrangian method. Atmos Environ. 45.30 (2011) 5376-5384.
[33] F. Zhan, D. Zhuang, G. Ding, J. Tang, Numerical model of particle deposition on fin surface of heat exchanger. Int J Refrig. 72 (2016) 27-40.
[34] D. Taler, P. Ocłoń, Determination of heat transfer formulas for gas flow in fin-and-tube heat exchanger with oval tubes using CFD simulations. Chem Eng Process Process Intensif. 83 (2014) 1-11.
[35] Y. P. Chen, Y. J. Sheng, C. Dong, J.F. Wu, Numerical simulation on flow field in circumferential overlap trisection helical baffle heat exchanger. Appl Therm Eng. 50.1 (2013) 1035-1043.
[36] T. Ma, Q.W. Wang, M. Zeng, Y.T. Chen, Y, Liu, V. Nagarajan, Study on heat transfer and pressure drop performances of ribbed channel in the high temperature heat exchanger. Appl Therm Eng. 99 (2012) 393-401.
[37] V. Yakhot, S. A. Orszag, Renormalization group analysis of turbulence. I. Basic theory. J Sci Comput. 1.1 (1986) 3-51.
[38] T.H. Shih, W.W. Liou, A. Shabbir, Z. Yang, J. Zhu, A new k-ϵ eddy viscosity model for high Reynolds number turbulent flows. Comput Fluids. 24.3 (1995) 227-238.
[39] F. R. Menter, Two-equation eddy-viscosity turbulence models for engineering applications. AIAA J. 32.8 (1994) 1598-1605.
[40] A.Z. Al-Garni, M. Tozan, W. G. Abdelrahman. Graphical techniques for managing field failures of aircraft systems and components. J Aircraft. 46.2 (2009) 608-616.
[41] M. R. Sippola, W. W. Nazaroff. Particle deposition from turbulent flow: Review of published research and its applicability to ventilation ducts in commercial buildings. (2002).
[42] A. R. McFarland, H. Gong, A. Muyshondt, W.B. Wente, N.K. Anand, Aerosol deposition in bends with turbulent flow. Environ Sci Technol. 31.12 (1997) 3371-3377.
[43] W. C. Reynolds, Fundamentals of turbulence for turbulence modeling and simulation. Stanford Univ Ca Dept of Mechanical Engineering. (1987)
[44] ANSYS Inc. 2011. "ANSYS fluent theory guide, Release 14.0" http://www.ansys.com.
[45] A. Li, G. Ahmadi, Dispersion and deposition of spherical particles from point sources in a turbulent channel flow. Aerosol Sci Technol. 16. 4 (1992) 209-226.
[46] T. Lin, G. Ahmadi, Particle deposition in turbulent duct flows-Comparisons of different model predictions. J Aerosol Sci. 38.4 (2007) 377-397.
[47] C. Chen, C.H. Lin, D. Wei, Q. Chen, Modeling particle deposition on the surfaces around a multi-slot diffuser. Build Environ. 107 (2016) 79-89.
[48] N. Gao, J. Niu, Q. He, T. Zhu, J. Wu, Using RANS turbulence models and Lagrangian approach to predict particle deposition in turbulent channel flows. Build Environ. 48 (2012) 206-214.
[49] H. Jiang, L. Lu, K. Sun, Experimental study and numerical investigation of particle penetration and deposition in 90 bent ventilation ducts. Build Environ. 46.11 (2011) 2195-2202.
[50] Y. Wang, P. W. James, On the effect of anisotropy on the turbulent dispersion and deposition of small particles. Int J Multiphas Flow. 25.3 (1999) 551-558.
[51] K. Jiao, H. Sun, X. Li, H. Wu, E. Krivitzky, T. Schram, L.M. Larosiliere, Numerical simulation of air flow through turbocharger compressors with dual volute design. Appl Energ. 86.11 (2009) 2494-2506.
[52] M. Coroneo, G. Montante, A. Paglianti, F. Magelli, CFD prediction of fluid flow and mixing in stirred tanks: Numerical issues about the RANS simulations. Comput Chem Eng. 35.10 (2011) 1959-1968.

[53] J. Galindo, P. Fajardo, R. Navarro, L.M. García-Cuevas, Characterization of a radial turbocharger turbine in pulsating flow by means of CFD and its application to engine modeling. Appl Energ. 103 (2013) 116-127.
[54] S. Elghobashi. On predicting particle-laden turbulent flows. Applied scientific research 52.4 (1994): 309-329.
[55] L.Tian, G. Ahmadi, Particle deposition in turbulent duct flows-comparisons of different model predictions. J Aerosol Sci, 38.4 (2007). 377-397.
[56] G. F. G. Bezemer, Particle deposition and clearance from the respiratory tract (Master's thesis). University of Utrecht, the Netherlands (2009).
[57] R. Yang, R. Liu, Z. Tao, Z. Lei, Kinematic characteristics and thermophoretic deposition of inhalable particles in turbulent duct flow. Chinese J Chem Eng 16.2 (2008) 192-197.
[58] M. Kang, H. J. Cho, H. Kwak, K. Park, Evaluation of Particle Bounce in Various Collection Substrates to be Used as Vaporizer in Aerosol Mass Spectrometer. Aerosol Sci Technol. 49. 5 (2015) 332-339.
[59] B. M. Matthew, A. M. Middlebrook, T. B. Onasch, Collection efficiencies in an Aerodyne Aerosol Mass Spectrometer as a function of particle phase for laboratory generated aerosols. Aerosol Sci Technol. 42. 11 (2008) 884-898.
[60] S. W. Stein, B. J. Turpin, X. Cai, P. F. Huang, P. H. Mcmurry, Measurements of relative humidity-dependent bounce and density for atmospheric particles using the DMA-impactor technique. Atmos Environ. 28. 10 (1994) 1739-1746.
[61] A.Virtanen, J. Joutsensaari, T. Koop, J. Kannosto, P. Yli-Pirilä, J. Leskinen, J.M. Mäkelä, J.K. Holopainen, U. Pöschl, M. Kulmala, D. R. Worsnop, An amorphous solid state of biogenic secondary organic aerosol particles. Nature, 467. 7317 (2010) 824.